Sensors and Materials, Vol. 36, No. 7 (2024) 2685–2704
MYU Tokyo

S & M 3695

Soft-thresholding Alternating Minimization Optimization Algorithm for Turntable-free Calibration Based on the Miniature Inertial Measurement Unit

Xiaowen Cai, Fengjiao Guo, Qiaoting Gong,
Daifeng Zhang, Yangzhuo Chen,* and Pinchun Li

School of Automation and Electronic Information, Xiangtan University, Xiangtan, Hunan 411105, China

(Received April 18, 2024; accepted July 2, 2024)

Keywords: device calibration, multiposition calibration, nonlinear optimization, convex optimization design MIMU

The micro inertial measurement unit (MIMU) is widely used in various fields such as aerospace, automotive industry, smartphones, and wearable devices. Field calibration is the key to ensuring measurement accuracy and reliability. To address the complex problem of solving calibration parameters for MIMU system errors in nonlinear optimization calibration methods, an alternating minimization algorithm based on soft thresholding updates was proposed in this paper. An accelerometer error model was established regarding gravity, and the gyroscope error model was established on the basis of the calibrated acceleration and rotation angular velocity in this method. Finally, the error models were used in convex optimization to design a simplified solution process. Compared with the Gauss–Newton algorithm, the scale factor calibration accuracy was improved by one order of magnitude, and in the nonorthogonal error and bias error calibration, the accuracy was improved by one to two orders of magnitude. Compared with the calibration method using a high-precision turntable with an accuracy of 0.001 °/s, the proposed method achieved an accuracy of 10^{-3} through manual calibration. It can still maintain stability with initial values of different orders of magnitude, and ultimately, the global optimal solution for the error was obtained.

1. Introduction

With the rapid development of the microelectromechanical system (MEMS), the MEMS micro inertial measurement unit (MIMU) has gained significant attention owing to its small size, low cost, and light weight. It plays an irreplaceable role in various applications, such as indoor positioning systems, smartphones, small unmanned aerial vehicles (UAVs), and inertial guidance systems. However, the inertial devices used in MIMU devices are subject to various error sources, such as bias, scale factor, and nonorthogonal installation errors, originating from manufacturing processes and assembly. These error sources severely affect the measurement

*Corresponding author: e-mail: 2138127686@qq.com
https://doi.org/10.18494/SAM5077

ISSN 0914-4935

accuracy of the MIMU and ultimately reduce the navigation accuracy. There are two main approaches for improving the accuracy of inertial devices: 1) improve the MIMU manufacturing processes and 2) implement error compensation and calibration techniques. With the continuous development of manufacturing processes, the manufacturing accuracy of MIMU has reached a bottleneck, making further improvements difficult owing to cost limitations. Traditional MIMU calibration methods typically require precision instruments and experimental equipment, such as high-precision turntables, to obtain the positional data of inertial devices for solving various error coefficients. However, these methods involve complex experimental procedures and expensive turntable equipment, making them unsuitable for low-cost inertial measurement unit (IMU) or real-time calibration applications.

The commonly used calibration methods without turntables include nonlinear optimization-based calibration,[1,2] recursive least squares-based calibration,[3,4] and Kalman filter calibration based on error equations.[5–7] In research on nonlinear-optimization-based calibration methods, Lötters *et al*.[8] proposed the model observation method, which converts the accelerometer calibration problem into a nonlinear optimization problem. Skog and Händel[9] utilized the principle that the norm of accelerometer and gyroscope measurements equals the applied force and rotation rate, respectively, to construct a cost function that achieves a mean square error of the sensor error parameters within 8 dB of the Cramér–Rao bound. Syed *et al*.[10] discussed the calibration problem of an IMU in a GPS/inertial navigation system (INS) integrated navigation system and extended the multiposition calibration method proposed by Shin and El-Sheimy,[11] including the calibration of the gyroscope scale factor and nonorthogonal installation error. Frosio *et al*.[12] employed the Newton method to solve the self-calibration problem of a triaxial accelerometer and quantitatively evaluated the calibration algorithm using a vision-based motion capture system. Qureshi and Golnaraghi[13] optimized the cost function of an accelerometer by the Newton method, carried out a simple rotation calibration of a gyroscope, and obtained high-precision calibration results. In addition, in solving nonlinear optimization calibration problems, intelligent optimization algorithms such as particle swarm optimization,[14,15] genetic algorithms,[16] and fruit fly optimization algorithms[17] are also commonly used, providing new insights for nonlinear-optimization-based calibration methods.

A summary of the MIMU turntable-free calibration schemes based on nonlinear optimization methods is shown in Table 1. The Newton-type algorithm is commonly used to optimize error parameters when solving MIMU calibration models. However, these methods involve the calculation of the Hessian matrix and matrix inversion, which can be computationally expensive and even difficult to compute, often leading to matrix singularity issues.[12,13] Although intelligent optimization algorithms can avoid matrix singularity problems, their accuracy is low, and it is easy for them to diverge.[16] Additionally, because of the nonconvex nature of the calibration error equation, there are multiple local minima in the calibration equation. The aforementioned algorithms can only produce good results when the initial values are close to the true values and fail to achieve the global optimum, which reduces the calibration accuracy.[14,16] Therefore, it is crucial to obtain the global optimal solution of the MIMU calibration parameters and reduce the computational complexity to improve the calibration accuracy.

Table 1
Characteristics of nonlinear optimization calibration schemes.

Author	Parameters and sensors	Method	Existing problems
Lötters *et al*.[8]	b, S, A	Quasistatic random motion for accelerometer calibration	Unable to calibrate K. The setting of the quasistatic threshold is arbitrary.
Skog and Händel[9]	b, S, K, A, G (single-axis turntable)	Newton iteration algorithm for estimation of parameter	No description of the gyroscope calibration process; unresolved sensor-to-sensor calibration
Frosio *et al*.[12]	b, S, K, A	Newton iteration algorithm for accelerometer calibration	Uncalibrated gyroscope; low accuracy; high computational complexity
Qureshi and Golnaraghi[13]	b, S, K, A, G	Newton's method and standard least squares algorithm	Uncalibrated gyroscope K. Matrix singularity issues can easily occur.
Poddar and Kumar[15]	b, S, K, A	Adaptive particle filter algorithm	Inaccurate estimation of K; prone to getting stuck in local optima
Cui *et al*.[16]	b, S, K, A, G (three-axis turntable)	Genetic algorithm used to estimate parameters	Low accuracy of S estimation; prone to getting stuck in local optima

Note: b—bias; S—scale factor; K—nonorthogonal error; A—accelerometer; G—gyroscope.

The main research content of this paper includes the following:

- To address the problem of complex error parameter optimization in MIMU nonlinear optimization calibration methods, a norm-based convex optimization method is introduced to optimize the calibration error equations of the accelerometer and gyroscope to improve the calibration efficiency.
- An alternating minimalization algorithm with soft thresholding updates is proposed to solve the calibration error equations and obtain the global optimal solution for the error parameters. The aim of this approach is to simplify the estimation process and improve the calibration accuracy of MIMU systems.

The organization of the paper is as follows. In Sect. 2, we establish the error models for the accelerometer and gyroscope of the MIMU. In Sect. 3, the calibration cost functions for the accelerometer and gyroscope are constructed, and an alternating minimalization algorithm based on soft thresholding updates is proposed. In Sect. 4, the calibration experiments conducted using the Mti-1 MIMU are shown, and the results are analyzed. Section 5 shows the conclusions.

2. MIMU Error Model Establishment

2.1 Error analysis and model development of MEMS accelerometers

The primary errors of an accelerometer include offset, scale factor, and nonorthogonal mounting errors. To establish an accelerometer error model based on the angle between the coordinate and ideal axes, as well as the distance of the origin offset, a method of rotation followed by translation is employed. The coordinate axes are rotated to align with the ideal axes, and then all three axes are translated to align with the ideal origin. Finally, proportional scaling is applied. The output data model of the accelerometer is established as follows:

$$a^s = S_a(Ka_b^s \cdot a^b + \nabla_a^s) = S_a' \cdot a^b + \nabla_a^v, \tag{1}$$

where

$$Ka_b^s = \begin{bmatrix} \cos(\theta_{xy})\cos(\theta_{xz}) & -\cos(\theta_{yx})\sin(\theta_{yz}) & \sin(\theta_{zy}) \\ \sin(\theta_{xz}) & \cos(\theta_{yx})\cos(\theta_{yz}) & -\cos(\theta_{zy})\sin(\theta_{zx}) \\ -\cos(\theta_{xz})\sin(\theta_{xy}) & \sin(\theta_{yx}) & \cos(\theta_{zx})\cos(\theta_{zy}) \end{bmatrix},$$

a^s and a^b represent the projection of the acceleration on the nonorthogonal coordinate system s and that on the orthogonal coordinate system b, respectively. S_a is a diagonal matrix whose elements S_{ax}, S_{ay}, and S_{az} on the diagonal are the scale factors of the three axes of the triaxial accelerometer. Ka_b^s is the transformation matrix from coordinate system b to coordinate system s. θ_{ij} represents the rotation angle of the i-axis of coordinate system b around the j-axis, and ∇_a^s represents the bias vector of acceleration in coordinate system s, which is a column matrix with three elements of ∇_{ax}^s, ∇_{ay}^s, and ∇_{az}^s, including $\nabla_a^v = S_a \cdot \nabla_a^s$, where $S_a' = S_a \cdot Ka_b^s$.

Because of nonorthogonal mounting error, the angles are all small, allowing the conversion matrix of the coordinate system to be rewritten in the form of a lower triangular matrix.

$$Ka_{bL}^s = \begin{bmatrix} 1 & 0 & 0 \\ -\sin(\theta_{xz}) & 1 & 0 \\ \sin(\theta_{xy}) & \sin(\theta_{yx}) & 1 \end{bmatrix} \tag{2}$$

The conversion model for transforming the acceleration data from the nonorthogonal coordinate system s to the orthogonal coordinate system b can be expressed as

$$a^b = (Ka_{bL}^s)^{-1}((S_a)^{-1}a^s - \nabla_a^s) = (S_a Ka_{bL}^s)^{-1}(a^s - S_a\nabla_a^s) = Ka \cdot (a^s - \nabla_a^v), \tag{3}$$

where

$$Ka = \begin{bmatrix} K_{xx} & 0 & 0 \\ K_{xz} & K_{yy} & 0 \\ K_{xy} & K_{yx} & K_{zz} \end{bmatrix}, \nabla_a^v = \begin{bmatrix} \nabla_{ax} \\ \nabla_{ay} \\ \nabla_{az} \end{bmatrix}, a^b = \begin{bmatrix} a_x^b \\ a_y^b \\ a_z^b \end{bmatrix}, a^s = \begin{bmatrix} a_x^s \\ a_y^s \\ a_z^s \end{bmatrix}. \tag{4}$$

2.2 Error analysis and model establishment of MEMS gyroscope

The process of establishing the gyroscope error model is similar to that of the accelerometer error model. The mounting, calibration factor, and bias errors of the gyroscope are considered. The data output model of the gyroscope is given by

$$w^s = S_g(Kg_b^s w^b + \nabla_g^s) = S' \cdot w^b + \nabla^v, \tag{5}$$

where w^s and w^b represents the projection of angular velocity in the nonorthogonal coordinate system s and that in the orthogonal coordinate system b, respectively. S_g represents the gyroscope scale factor matrix. Kg_b^s represents the gyroscope coordinate system transformation matrix. ∇_g^s represents the gyroscope bias vector in the system s.

The coordinate system transformation matrix is rewritten as a lower triangular matrix. Therefore, the transformation model for converting gyroscope data from the coordinate system to the orthogonal coordinate system s is

$$w^b = S'^{-1}(w^s - \nabla_g^v) = (S_g Kg_{bL}^s)^{-1}(w^s - \nabla_g^v) = Kg(w^s - \nabla_g^v), \tag{6}$$

where

$$Kg = \begin{bmatrix} K'_{xx} & 0 & 0 \\ K'_{xz} & K'_{yy} & 0 \\ K'_{xy} & K'_{yx} & K'_{zz} \end{bmatrix}, \nabla_g^v = \begin{bmatrix} \nabla_{gx} \\ \nabla_{gy} \\ \nabla_{gz} \end{bmatrix}, w^b = \begin{bmatrix} w_x^b \\ w_y^b \\ w_z^b \end{bmatrix}, w^s = \begin{bmatrix} w_x^s \\ w_y^s \\ w_z^s \end{bmatrix}. \tag{7}$$

3. Alternating Minimization Calibration Method Based on the Soft Thresholding Update

3.1 Calibration of acceleration mode observation method based on L1 norm

The cost function for traditional accelerometer calibration is typically modeled as a nonconvex smoothing function,[1,2,9,13] which has multiple local minima during iterative solving and complex calculations, leading to decreased solution accuracy. Therefore, by leveraging the principle that the sum of accelerometer vectors equals the local gravitational acceleration vector under static conditions, the cost function for accelerometer calibration can be expressed as

$$L(\theta_a) = \arg\min\left(\sum_{i=1}^{n} \left| \left\| a_i^b \right\|^2 - \|g\|^2 \right| \right), \tag{8}$$

where $\theta_a = \left[K_{xx}, K_{yy}, K_{zz}, K_{xz}, K_{xy}, K_{yx}, \nabla_{ax}, \nabla_{ay}, \nabla_{az} \right]$ is the parameter to be calibrated, n is the number of acquired accelerations, a_i^b is the projection of the i-th acceleration value on system b, and g is the local gravity vector that can be calculated in accordance with the local geographic longitude, latitude, and altitude $g = \left[g_x \quad g_y \quad g_z \right]^T$.

As the MIMU has multiple sources of error and its actual acceleration at rest is not equal to the local gravitational acceleration, in this paper, we propose a cost function for accelerometer calibration that is formulated as a convex function in the L1-norm form devoid of singular

points. By solving the convex optimization problem corresponding to the L1-norm, it becomes possible to attain the global optimal solution for the original nonconvex optimization problem, effectively circumventing local minimum traps and reducing computational complexity compared with traditional models.

3.2 Gyroscope calibration based on acceleration correction values

By combining the corrected acceleration in the previous stationary state with the angular velocity generated by rotation and employing an inertial navigation algorithm to update the MIMU attitude, it becomes possible to determine the acceleration in the current stationary state.

$$a_{k+1} = C_b^n \hat{a}_k, \tag{9}$$

where $\hat{a}_k$ is the corrected output value of the accelerometer for the k-th static state, C_b^n is the coordinate rotation matrix, and a_{k+1} is the IMU acceleration in the $(k + 1)$-th static state.

According to the inertial solution, the acceleration in the current static state should be equal to the accelerometer measurement at the previous moment, and the error function for calibrating the gyroscope should be constructed. Assuming the availability of M sets of inertial data comprising dynamic and stationary intervals, the cost function for gyroscope calibration is constructed as

$$\theta^g = \arg\min \sum_{k=2}^{M} \left| \|a_k\|^2 - \|\hat{a}_{k-1}\|^2 \right|, \tag{10}$$

where a_k is the IMU acceleration in the k-th static state and $\hat{a}_{k-1}$ is the corrected output value of the accelerometer for the $(k - 1)$-th static state.

3.3 Alternating minimization optimization algorithm based on soft thresholding update

For objective function (8), set $y = \left\| Ka \cdot a^s - Ka \cdot \nabla_a^v \right\|^2 - \|g\|^2$ to construct a constrained optimization problem:

$$\begin{cases} \min \sum_{i=1}^{n} |y_i|, \\ \text{s.t. } y_i = \left\| Ka \cdot a_i^s - Ka \cdot \nabla_a^v \right\|^2 - \|g\|^2. \end{cases} \tag{11}$$

The constrained optimization problem (11) exhibits strong convexity. Introducing the Lagrange multiplier $\lambda_k{}^T$ to construct the Lagrange function for problem (11) gives

$$L(Ka,\nabla_a^v,y,\lambda)=\|y\|_1-\lambda^T\left(y-\begin{bmatrix}\left\|Ka\cdot(a_1^s-\nabla_a^v)\right\|^2-\|g\|^2\\ \vdots\\ \left\|Ka\cdot(a_n^s-\nabla_a^v)\right\|^2-\|g\|^2\end{bmatrix}\right). \tag{12}$$

The alternating minimization algorithm is used to fix y in the Lagrange function (12), and Ka and ∇_a^v are alternately minimized to obtain the optimal solutions of Ka and ∇_a^v, respectively. For the solution of y, the following problem form is obtained using the regularization problem (11):

$$\begin{cases}\min\limits_{y}\ \mu\|y\|_1+\dfrac{1}{2}\|y-C_k\|_2^2,\\ \text{s.t. } y_i=\left\|Ka\cdot a_i^s-Ka\cdot\nabla_a^v\right\|^2-\|g\|^2,\end{cases} \tag{13}$$

where $\mu > 0$ is the regularization parameter and

$$C_k=\begin{bmatrix}\left\|Ka^{(k)}\cdot(a_1^s-\nabla_a^{v(k)})\right\|-\|g\|\\ \vdots\\ \left\|Ka^{(k)}\cdot(a_n^s-\nabla_a^{v(k)})\right\|^2-\|g\|^2\end{bmatrix}.$$

When solving optimization problem (13) and its corresponding reformulation, the iterated soft-thresholding (IST) operator is used to construct the corresponding optimization algorithm. Because of the suitability of the alternating direction method of multipliers (ADMM) for solving separable convex optimization problems and its simplicity in iterations, we here adopt the IST operator within the ADMM framework to solve problem (13) and obtain the optimal value. Consequently, the steps for solving the accelerometer error equation using the alternating iterative algorithm based on soft-thresholding updates can be given as below.

Step 1: The augmented Lagrange function of problem (11) can be written as

$$\begin{aligned}y^{(k+1)}&=\arg\min_y\left\{\|y\|_1-\lambda_k^T(y-C_k)+\frac{\rho}{2}\|y-C_k\|_2^2\right\}\\ &=\arg\min_y\left\{\|y\|_1+\frac{\rho}{2}\|y-b_k\|_2^2+\hat{C}_k\right\},\end{aligned} \tag{14}$$

where C_k is a constant, $b_k = \lambda_k/\rho + C_k$, $\rho > 0$ is a penalty factor, and $\hat{C}_k=-\lambda_k/2\rho$ is a constant term. The optimization problem (14) is equivalent to

$$y^{(k+1)} = \arg\min_{y} \left\{ \left\| y - b_k \right\|_2^2 + \frac{2}{\rho} \left\| y \right\|_1 \right\}. \tag{15}$$

Applying IST to solve the optimization problem (15), the iterative steps of y can be obtained as

$$y^{(0)} = 0,$$
$$y^{(k+1)} = \begin{cases} y^{(k)} - 2t_k \cdot \left(y^{(k)} - b_k \right) - \frac{2}{\rho} \cdot t_k, & y^{(k)} > \frac{2}{\rho} \cdot t_k + 2t_k \cdot \left(y^{(k)} - b_k \right), \\ y^{(k)} - 2t_k \cdot \left(y^{(k)} - b_k \right) + \frac{2}{\rho} \cdot t_k, & y^{(k)} < -\frac{2}{\rho} \cdot t_k + 2t_k \cdot \left(y^{(k)} - b_k \right), \\ 0, & -\frac{2}{\rho} \cdot t_k + 2t_k \cdot \left(y^{(k)} - b_k \right) \le y^{(k)} \le \frac{2}{\rho} \cdot t_k + 2t_k \cdot \left(y^{(k)} - b_k \right), \end{cases} \tag{16}$$

where $t_k = 1/L_f$ is the step size and L_f is the Lipschitz constant.

Step 2: In the Lagrange function (12), Ka is minimized and solved using the gradient descent algorithm. The iterative format Ka is

$$Ka^{(k+1)} = Ka^{(k)} - \alpha_k \cdot \nabla_{Ka} L, \tag{17}$$

where α_k is the iteration step size and $\nabla_{Ka} L$ is the gradient obtained by the Lagrange function for Ka and is

$$\nabla_{Ka} L = \sum_{i=1}^{n} \lambda_i \cdot Ka \cdot (a_i^s - \nabla_a^{v(k)}) \cdot (a_i^s - \nabla_a^{v(k)})^T. \tag{18}$$

Step 3: To minimize ∇_a^v in the Lagrange function (12) using the gradient descent algorithm, the iterative format ∇_a^v is given by

$$\nabla_a^{v(k+1)} = \nabla_a^{v(k)} - \beta_k \cdot \nabla_{\nabla_a^v} L, \tag{19}$$

where β_k is the iteration step size and $\nabla_{\nabla_a^v} L$ is the gradient obtained by the Lagrange function for ∇_a^v.

$$\nabla_{\nabla_a^v} L = -\sum_{i=1}^{n} \lambda_i \cdot (Ka^{(k+1)})^T \cdot Ka^{(k+1)} \cdot \left(a_i^s - \nabla_a^v \right). \tag{20}$$

Using the Armijo line search to update the step size α_k, β_k, the Armijo criterion, ensures that each step of the iteration is fully reduced if

$$L(Ka^{(k)} - \alpha_k \cdot \nabla_{Ka} L) \le L(Ka^{(k)}) + \sigma \cdot \alpha_k \cdot (\nabla_{Ka} L)^T \cdot (-\nabla_{Ka} L), \tag{21}$$

$\nabla_{\nabla_a^v} L$ is the gradient obtained by the Lagrange function to ∇_a^v. The step size α_k satisfies the Armijo criterion, where $\sigma \in (0, 0.5)$ is a constant: $\alpha_k = a^m, (m = 0, 1, 2, ...), a \in (0,1)$. Similarly, the variable β_k can be updated.

Step 4: Iteratively update the Lagrange multiplier λ as

$$\lambda^{(k+1)} = \lambda^{(k)} - \gamma_k \left(y^{(k+1)} - \begin{bmatrix} \left\| Ka^{(k+1)} \cdot (a_1^s - \nabla_a^{v(k+1)}) \right\|^2 - \|g\|^2 \\ \vdots \\ \left\| Ka^{(k+1)} \cdot (a_n^s - \nabla_a^{v(k+1)}) \right\|^2 - \|g\|^2 \end{bmatrix} \right), \tag{22}$$

where γ_k is the step size, which is updated as $\gamma_{k+1} = \gamma_k \cdot \rho$, $\rho \in [2,10]$, and $\gamma_0 \in (1,2)$.

After calibrating the accelerometer, the optimized solution for the gyroscope calibration parameters is obtained by using the alternating minimization algorithm based on soft thresholding updates to minimize the gyroscope calibration cost function (10).

4. Experimental Verification and Results of Analysis

The MTI-1 IMU module of XSENS Company as shown in Fig. 1 is used for experimental verification. The operating voltage is 3.3 V. A horizontal marble platform is used to ensure the accuracy of the measurements, reduce human error, and ensure the consistency of the measurement process. The technical specifications are shown in Table 2.

4.1 Calibration path scheme design

In the scenario where the navigation coordinate system aligns with the east–north–up (ENU) frame, the calibration path scheme is presented in Table 3, and the initial static attitude of the IMU is illustrated in Fig. 3. The marble platform has high flatness and stability, which can ensure that the MIMU is not affected by the uneven surface of the platform during calibration, thereby improving the calibration accuracy. Therefore, the experiment was carried out on a marble platform. As shown in Fig. 2, the IMU is fixed in a simple cube frame for data acquisition, and a total of 10 groups of experimental data are collected. Following the set calibration path, each set of experimental data consists of 12 rotating and stationary data points at different positions, with the sensor being manually rotated.

First, the cube frame is placed on the marble platform to collect static data for initialization; Second, the cube frame is rapidly rotated around the positive direction of the *y*-axis at 0, 90, 180, and 270°, around the positive direction of the *x*-axis at 0, 90, 180, and 270°, and finally around the positive direction of the *z*-axis at 0, 90, 180, and 270°. After each rotation, the sensor is placed on the marble platform for 3 s to collect data, after which the next rotation begins. Finally,

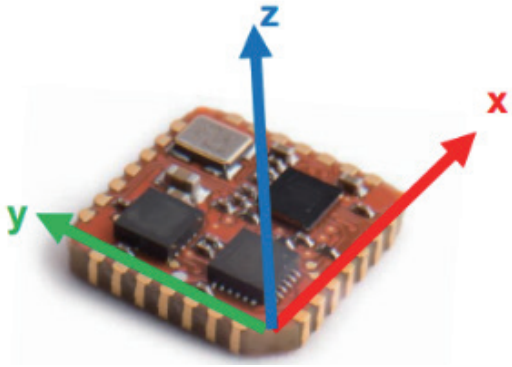

Fig. 1. (Color online) Xsens MTI-1 IMU.

Fig. 2. (Color online) Horizontal marble platform.

Table 2
MTI-1 IMU technical indices.

MTI-1 IMU	
Accelerometer range	±16 g
Zero-bias stability of accelerometer	0.1 mg
Gyroscope range	±2000 °/s
Zero-bias stability of gyroscope	10 °/h
Magnetometer range	±0.8 G
Magnetometer noise intensity	200 μG

a total of 12 sets of static data and 11 sets of rotational data were collected at 12 different positions for error calibration. The calibration paths for the 12 positions are shown in Table 3.

To distinguish between static and dynamic data from accelerometers and gyroscopes, a variance-based static detection algorithm is adopted, utilizing acceleration data to construct a static detection operator. The acceleration data (a_k^x, a_k^y, a_k^z) at any time k are taken as the center, an acceleration interval is set with a length of N, and the variance σ_k^2 is calculated.

$$\sigma_k^2 = std_N(a_k^x) + std_N(a_k^y) + std_N(a_k^z), \tag{23}$$

where $std_N(x)$ represents the variance operator of the three-axis acceleration. The variance threshold λ is set, and the IMU motion state is determined on the basis of the acceleration variance at time k. When the variance σ_k^2 is less than the threshold, the time is determined to be in a stationary state; when the variance σ_k^2 is greater than the threshold, the moment is determined to be in a motion state.

First, the MTI-1 IMU module was placed on a marble platform in a static position aligned with the northeast direction, and initial static data were collected for 1 min at a sampling frequency of 100 Hz. Second, the IMU was rapidly rotated to the next position on the designated path and then kept stationary, holding the static state for 3 s after each rotation until data from 12 positions were collected. This process was repeated 10 times to gather 10 sets of valid data. Third, for each set of data, 12 stationary interval data points and 11 rotating interval data points

Table 3
Design table for the twelve-position calibration path.

Position	Rotation	Illustration
1	60 s of stationary period.	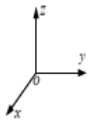
2	Rotate around the *y*-axis by +90°, followed by a stationary period of 3 s.	
3	Rotate around the *y*-axis by +180°, followed by a stationary period of 3 s.	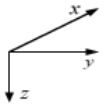
4	Rotate around the *y*-axis by +270°, followed by a stationary period of 3 s.	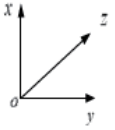
5	Rotate around the *x*-axis by +90°, followed by a rotation around the *y*-axis by +90° and then a stationary period of 3 s.	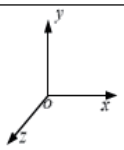
6	Rotate around the *x*-axis by +90°, followed by a stationary period of 3 s.	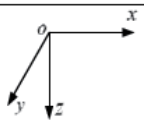
7	Rotate around the *x*-axis by +180°, followed by a stationary period of 3 s.	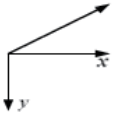
8	Rotate around the *x*-axis by +270°, followed by a stationary period of 3 s.	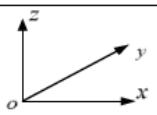
9	Rotate around the *y*-axis by +90°, followed by a rotation around the *x*-axis by +90°and then a stationary period of 3 s.	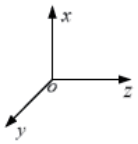
10	Rotate around the *z*-axis by +90°, followed by a stationary period of 3 s.	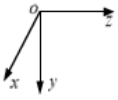
11	Rotate around the *z*-axis by +180°, followed by a stationary period of 3 s.	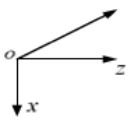
12	Rotate around the *z*-axis by +270°, followed by a stationary period of 3 s.	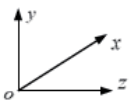

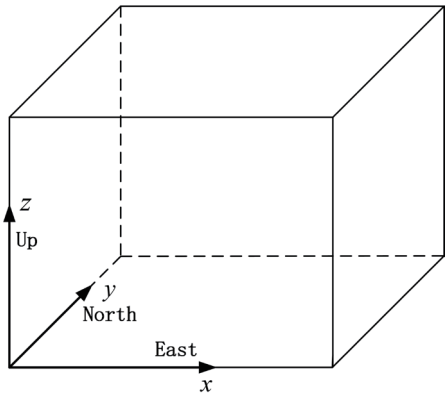

Fig. 3. Initial static state of the IMU.

were collected according to the set calibration path. Finally, a static detector was used to distinguish between the static data for accelerometer calibration and the rotation data for gyroscope calibration. Some sample data formats are listed in Table 4, where Packet Counter represents the number of data points; Acc_X, Acc_Y, and Acc_Z represent the acceleration data of the *x*-, *y*-, and *z*-axes, and Gyr_X, Gyr_Y, and Gyr_Z represent the angular velocity data of the *x*-, *y*-, and *z*-axes, respectively.

In Fig. 4, the static detector is depicted as a black square wave, where a high level indicates an interval classified as static. There are 12 static intervals and 11 dynamic intervals, which are consistent with the actual sampling conditions. The simulation results are simulated in MATLAB by collecting data through serial ports.

4.2 Calibration results and analysis

A comparison of two different experimental scenarios is conducted to evaluate the proposed algorithm: high-precision turntable calibration and calibration using the Gauss–Newton algorithm. The reasons for choosing these scenarios are as follows.

First, high-precision turntables are widely recognized as reliable calibration tools that enable the accurate measurement and calibration of sensor performance. By mounting the sensors on a precisely controlled turntable, predefined angular velocities and angles can be applied. The outcomes obtained from turntable calibration are typically regarded as accurate reference values.

Second, the Gauss–Newton algorithm, a widely adopted optimization algorithm, is employed as a reference method for parameter estimation and nonlinear least squares problem solving. The parameter values are iteratively adjusted to minimize the difference between the objective function (calibration cost function) and observed values. This approach is commonly used for calibrating different error parameters of accelerometers and demonstrates effective performance in scale factor calibration. However, this approach is prone to becoming stuck in local optima and tends to yield moderate results in calibrating nonorthogonal and bias errors.

Table 4
IMU data formats.

Packet Counter	Acc_X	Acc_Y	Acc_Z	Gyr_X	Gyr_Y	Gyr_X
03366	0.032724	−0.077869	9.774956	−0.002386	−0.002581	0.001581
03367	0.027340	−0.089129	9.763243	−0.003562	−0.002573	0.002013
03368	0.037307	−0.091866	9.794288	−0.000690	−0.003613	0.002125

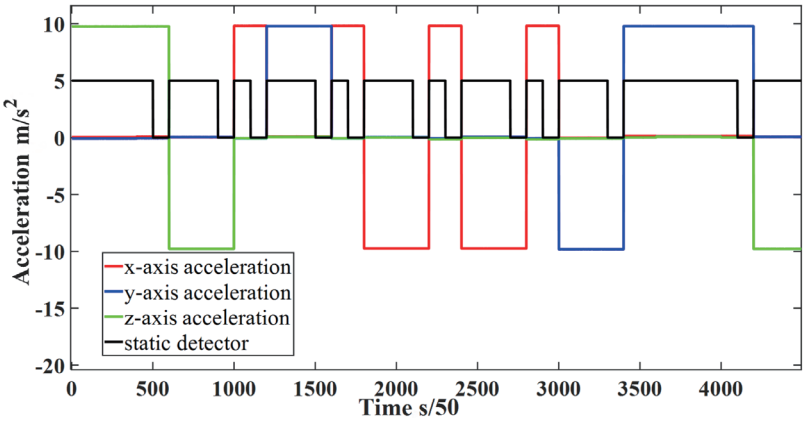

Fig. 4. (Color online) Static detector result.

The error and bias matrices for the accelerometer and gyroscope are calculated as

$$Ka = (S_a Ka_{bL}^s)^{-1} = \begin{bmatrix} 1.0218 & 0 & 0 \\ 0.0020 & 1.0200 & 0 \\ 0.0002143 & 0.0011 & 1.0234 \end{bmatrix}, \tag{24}$$

$$\nabla_a^v = S_a \nabla_a^s = \begin{bmatrix} 0.0410 & -0.0049 & -0.0028 \end{bmatrix}^T \text{ m/s}^2, \tag{25}$$

$$Kg = (S_g Kg_{bL}^s)^{-1} = \begin{bmatrix} 57.2525 & 0 & 0 \\ -0.4066 & 57.4267 & 0 \\ -0.2624 & 0.2228 & 57.3658 \end{bmatrix}, \tag{26}$$

$$\nabla_g^v = S_g \nabla_g^s = \begin{bmatrix} -0.0011 & -0.0018 & -0.0014 \end{bmatrix}^T \text{ °/h}. \tag{27}$$

Using the GRS80 gravity model, the local gravity acceleration was calculated to be 9.80 m/s^2. For the high-precision turntable calibration scenario, the experimental results are presented in Tables 5 and 6. The turntable had an accuracy of ±0.001 °/s.

Using the proposed calibration method, the collected data from 10 experimental trials were subjected to iterative optimization to obtain the calibration error parameters for the accelerometer and gyroscope. The corresponding averages and standard deviations were calculated and are presented in Tables 7 and 8, respectively.

Table 5
Turntable calibration values for accelerometer error.

Error type		Error value	
Zero-bias error ∇_a^s (m/s^2)	0.0418975	−0.004965	−0.002915
Scale factor S_a	9.7869075	9.80403	9.771265
Nonorthogonal error Ka_{bL}^s	−0.001955	−0.000195	−0.001095

Table 6
Turntable calibration values for gyroscope error.

Error type		Error value	
Zero-bias error ∇_g^s (°/h)	0.0418975	−0.004965	−0.002915
Scale factor S_g	9.7869075	9.80403	9.771265
Nonorthogonal error Kg_{bL}^s	−0.001955	−0.000195	−0.001095

Table 7
Averages and standard deviations of accelerometer parameters.

Parameter	Turntable calibration	Average	Standard deviation
K_{xx}	1.0218	1.0228	0.00056
K_{yy}	1.0200	1.0210	0.0031
K_{zz}	1.0234	1.0244	0.00064
K_{xz}	0.0020	0.0021	0.0000504
K_{xy}	0.0002143	0.000234	0.0000176
K_{yx}	0.0011	0.0012	0.00011
∇_{ax} (m/s)	0.0410	0.0419	0.000604
∇_{ay} (m/s)	−0.0049	−0.0046	0.000166
∇_{az} (m/s)	−0.0028	−0.0026	0.0000918

Table 8
Averages and standard deviations of gyroscope parameters.

Parameter	Turntable calibration	Average	Standard deviation
K'_{xx}	57.2525	57.7764	0.2628
K'_{yy}	57.4267	58.0131	0.2060
K'_{zz}	57.3658	57.9057	0.2576
K'_{xz}	−0.4066	−0.4053	0.000932
K'_{xy}	−0.2624	−0.2618	0.000296
K'_{yx}	0.2228	0.2239	0.000426
∇_{gx} (°/h)	−0.0011	−0.0011	0.0000308
∇_{gy} (°/h)	−0.0018	−0.0016	0.000127
∇_{gz} (°/h)	−0.0014	−0.0012	0.0000873

The proximity between the average calibration values of the ten datasets and the calibration values obtained from the turntable demonstrates the high calibration accuracy achieved by the proposed method. Furthermore, the standard deviation of the calibration parameters being of the same order of magnitude indicates an excellent repeatability of the calibration results.

To validate the effectiveness of the algorithm in IMU calibration, both the proposed method and the Gauss–Newton algorithm are employed to solve the cost function for accelerometer and gyroscope calibrations, using different initial values for the iterations. A comparative analysis is

conducted to evaluate the calibration results. Compared with the Gauss–Newton algorithm, the proposed algorithm improves the scale factor calibration accuracy by one order of magnitude and achieves an accuracy improvement of one to two orders of magnitude in nonorthogonal and bias error calibrations.

The static data collected are compensated using the accelerometer calibration parameters provided in Table 9. The uncompensated and compensated acceleration values are shown in Fig. 5. The relative errors of the accelerometer calibration parameters are shown in Table 10. The standard deviation and root mean square error between these values and the local gravity acceleration are computed and presented in Table 11.

As shown in Fig. 5, the compensated acceleration amplitude is closer to the local gravity acceleration. Compared with the original data without compensation, the standard deviation of the acceleration data is reduced by one order of magnitude, and the root mean square error is reduced 46 times. The calibrated acceleration value has higher accuracy and data stability.

Using the compensated static acceleration and rotational angular velocity data for gyroscope calibration, both the proposed method and the Gaussian–Newton algorithm are employed to solve the gyroscope calibration cost function. The gyroscope calibration parameters are presented in Table 12, while the relative errors of the calibration parameters are displayed in Table 13.

Table 9
Accelerometer calibration parameters.

Parameter	Turntable calibration value	Proposed method		Gauss–Newton method	
		Initial value 1 (Uncompensated)	Initial value 2 (Compensated)	Initial value 1 (Uncompensated)	Initial value 2 (Compensated)
K_{xx}	1.0218	1.0201	1.0204	1.0101	1.0104
K_{yy}	1.0200	1.0201	1.0210	1.0309	1.0309
K_{zz}	1.0234	0.9889	0.9895	0.9867	0.9707
K_{xz}	0.0020	0.0020	0.0020	−0.0010	−0.0020
K_{xy}	0.0002143	0.0002096	0.0002264	0.0003237	0.0002061
K_{yx}	0.0011	0.0014	0.0012	0.0013	0.0015
∇_{ax} (m/s)	0.0410	0.0399	0.0392	0.0310	0.0340
∇_{ay} (m/s)	−0.0049	−0.0049	−0.0049	−0.0046	−0.0040
∇_{az} (m/s)	−0.0028	−0.00274	−0.00269	−0.0011	−0.0021

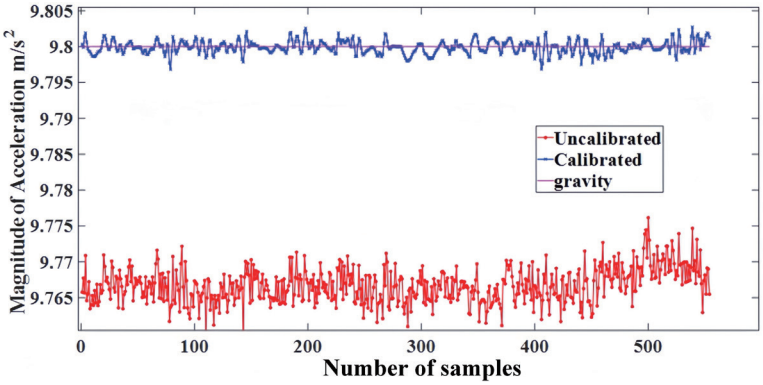

Fig. 5. (Color online) Acceleration data obtained before and after compensation.

Table 10
Relative error of accelerometer calibration parameters.

Parameter	Proposed method		Gauss–Newton method	
	Initial value 1 Relative error/%	Initial value 2 Relative error/%	Initial value 1 Relative error/%	Initial value 2 Relative error/%
K_{xx}	0.1664	0.1370	1.1450	1.1157
K_{yy}	0.0098	0.0980	1.0686	1.0686
K_{zz}	3.3711	3.3125	3.5861	5.1495
K_{xz}	0	0	150	200
K_{xy}	2.1932	5.6463	51.0499	3.8264
K_{yx}	27.2727	9.0909	18.1818	36.3636
∇_{ax} (m/s)	2.6829	4.3902	24.3902	17.0732
∇_{ay} (m/s)	0	0	6.1224	18.3673
∇_{az} (m/s)	2.1429	3.9286	60.7143	25

Table 11
Acceleration standard deviation and root mean square error before and after compensation.

	Standard deviation	Root mean error
Uncompensated	0.0025	0.033
Compensated	0.00091	0.0007

Table 12
Gyroscope calibration parameters.

Parameter	Turntable calibration value	Proposed method		Gauss–Newton method	
		Initial value 1	Initial value 2	Initial value 1	Initial value 2
K'_{xx}	57.2525	57.891	59.8587	57.4627	
K'_{yy}	57.4267	56.9350	63.1217	56.8914	
K'_{zz}	57.3658	57.165	62.3087	56.4951	
K'_{xz}	−0.4066	−0.4176	−0.3365	−0.3761	
K'_{xy}	−0.2624	−0.2535	−0.1841	−0.1279	—
K'_{yx}	0.2228	0.2013	0.3037	0.1903	
∇_{gx} (°/h)	−0.0011	−0.0015	−0.0011	−0.0017	
∇_{gy} (°/h)	−0.0018	−0.0017	−0.0022	−0.0011	
∇_{gz} (°/h)	−0.0014	−0.0013	−0.0011	−0.0012	

Table 13
Relative errors of gyroscope calibration parameters.

Parameter	Proposed method		Gauss–Newton method	
	Initial value 1 Relative error/%	Initial value 2 Relative error/%	Initial value 1 Relative error/%	Initial value 2 Relative error/%
K_{xx}	1.1152	4.5521	0.3671	
K_{yy}	0.8562	9.9170	0.9321	
K_{zz}	0.3500	8.6165	1.5178	
K_{xz}	2.7054	17.2405	7.5012	
K_{xy}	3.3918	29.8399	51.2576	—
K_{yx}	9.6499	36.3106	14.5871	
∇_{ax} (m/s)	9.0909	0	54.5455	
∇_{ay} (m/s)	5.5556	22.2222	38.8889	
∇_{az} (m/s)	7.1429	21.4286	14.2857	

The analysis of the calibration results in Tables 12 and 13 shows that for an initial value of 1, both algorithms successfully calibrate the gyro's error parameters. However, the proposed method outperforms the Gauss–Newton algorithm in terms of calibration accuracy, particularly in terms of nonorthogonal and bias error calibrations, where it achieves an improvement of one order of magnitude. For an initial value of 2, the Gauss–Newton algorithm fails to converge owing to matrix singularities during the iterative process, resulting in divergent calibration results. Conversely, the proposed algorithm is effective at calibrating the error parameters and achieves a higher calibration accuracy than does the Gauss–Newton algorithm, specifically in terms of bias error calibration under an initial value of 1. Compared with the Newton-class nonlinear optimization algorithm, the Jacobian matrix of the independent variable does not need to be calculated, which solves the problem that the traditional algorithm is difficult to calculate and falls into the local extreme value, and reduces the amount of computation.

To validate the accuracy of the gyroscope calibration results, the initial attitude angle is set to [0 0 0]. The angular velocity is compensated by the gyro calibration error parameter, and the attitude calculation results obtained before and after compensation are compared. The attitude calculation results are shown in Fig. 6, and the attitude angles calculated before and after a 50 s static interval are presented in Table 14.

Figure 6 depicts the variations in the pitch angle, roll angle, and heading angle of the uncompensated and compensated beams. The attitude angles calculated after calibration compensation exhibit relative stability, with a maximum pitch drift of 0.13°, a maximum roll drift of 0.20°, and a maximum yaw drift of 0.5° within 50 s. Overall, both the accuracy and the stability significantly improved.

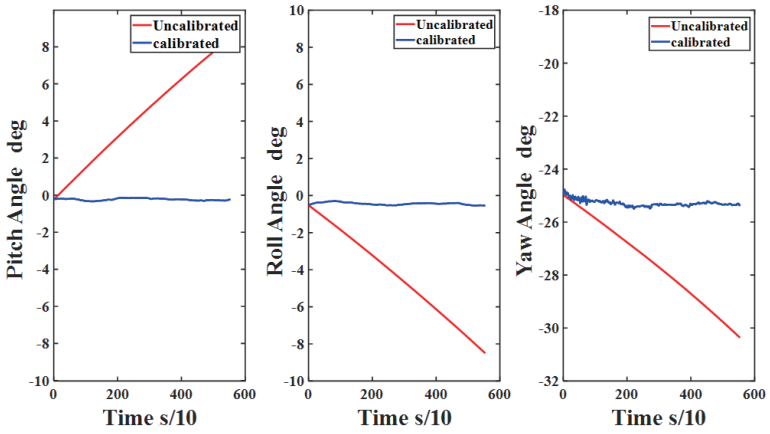

Fig. 6. (Color online) Attitude calculation results in the static state.

Table 14
Attitude angles calculated before and after calibration.

	Pitch/°	Roll/°	Yaw/°
Initial attitude angle	−0.21	−0.50	−24.9
Uncompensated attitude angle	8.47	−8.50	−30.39
Compensated attitude angle	−0.08	−0.70	−25.4
Uncompensated attitude angle error	8.67	8.00	5.49
Compensated attitude angle error	0.13	0.20	0.50

The experimental results provide evidence of successful accelerometer and gyroscope calibrations by effectively addressing bias, scale factor, and nonorthogonal mounting errors. The achieved accuracy is in agreement with that of turntable calibration. Following calibration, the root mean square error of the static acceleration decreases from 0.033 to 0.0007 degrees. Additionally, the proposed algorithm significantly reduces the pitch, roll, and yaw angle drifts by 98.5, 97.5, and 90.9%, respectively, within a specific timeframe. Furthermore, the algorithm exhibits robustness and adaptability to different initial input values, yielding calibration results close to the ground truth.

5. Conclusions

To address the challenges associated with nonlinear optimization calibration techniques, a convenient MIMU calibration method was proposed in this paper. The challenges included prolonged data collection time, complex calibration parameter models, and susceptibility to local optima. The error models of the accelerometer and gyroscope were developed as convex functions by using the L1-norm calibration cost function. This iterative approach enabled us to obtain the globally optimal solution for the error parameters, thereby significantly reducing the computational complexity involved in the calibration process. These findings underscore the suitability of low-cost IMU field calibration methods for the calibration of smartphones, microdrones, and wearable devices. This paper was focused mainly on mathematical theory, but testing in more practical scenarios will be conducted in the future.

Acknowledgments

This work was supported by the National Natural Science Foundation of China (Grant No. 62103348). This work was supported by the Key Project of Research and Development Plan of Hunan Province (Grant No. 2023GK2032).

References

1 X. Chen, Y. Liu, Y. Xu, S. Gou, S. Ma, and Z. Ullah: Measurement **191** (2022) 110672. https://doi.org/10.1016/j.measurement.2021.110672
2 D. Tedaldi, A. Pretto, and E. Menegatti: 2014 IEEE Int. Conf. Robotics and Automation (ICRA) (IEEE, 2014) 3042–3049. https://doi.org/10.1109/ICRA.2014.6907297
3 Z. Chen, H. Li, X. Du X, and J. Yan: 2018 IEEE Int. Conf. Mechatronics and Automation (ICMA) (IEEE, 2018) 533–538. https://doi.org/10.1109/ICMA.2018.8484627
4 L. Ye, Y. Guo, and S. W. Su: IEEE Trans. Instrumentation and Measurement **66** (2017) 2380 (accessed April 2016). https://doi.org/10.1109/TIM.2017.2706479
5 M. Dong, G. Yao, J. Li, and L Zhang: J. Intell. Rob. Syst. **100** (2020) 1015. https://doi.org/10.1007/s10846-020-01259-0
6 I. Costa-Carrapiço, B. Croxford, R. Raslan, and J. N. González: J. Build. Eng. **55** (2022) 104717. https://doi.org/10.1016/j.jobe.2022.104717
7 B. Wang, Q. Ren, Z. Deng, and M. Fu: IEEE Trans. Ind. Electron. **62** (2014) 2353. https://doi.org/10.1109/TIE.2014.2361671
8 J. C. Lötters, J. Schipper, P. H. Veltink, W. Olthuis, and P. Bergveld: Sens. Actuators, A **68** (1998) 221. https://doi.org/10.1016/S0924-4247(98)00049-1
9 I. Skog and P. Händel: XVII IMEKO World Congress (2006) 1–6. https://doi.org/10.1109/robot.2008.4543384

10 Z. F. Syed, P. Aggarwal, C. Goodall, X. Niu, and N. El-Sheimy: Meas. Sci. Technol. **18** (2007) 1897. https://doi.org/10.1088/0957-0233/18/7/016
11 E. H. Shin and N. El-Sheimy: Z. Vermess **127** (2002) 1. https://doi.org/10.1049/pbra017e_ch3
12 I. Frosio, F. Pedersini, and N. A. Borghese: IEEE Trans. Instrum. Meas. **58** (2008) 2034. https://doi.org/10.1109/TIM.2008.2006137
13 U. Qureshi and F. Golnaraghi: IEEE Sens. J. **17** (2017) 7479. https://doi.org/10.1109/JSEN.2017.2751572
14 S. Dhalwar, R. Kottath, V. Kumar, A. N. J. Raj, and S. Poddar: 2016 IEEE 1st Int. Conf. Power Electronics, Intelligent Control and Energy Systems (ICPEICES) (IEEE, 2016) 1–5. https://doi.org/10.1109/ICPEICES.2016.7853718
15 S. Poddar and A. Kumar: Measurement **147** (2019) 106849. https://doi.org/10.1016/j.measurement.2019.07.077
16 X. Cui, C. Liu, G. Shi, and Y. Jin: 2017 IEEE Int. Conf. Real-Time Computing and Robotics (RCAR) (IEEE, 2017) 240–245. https://doi.org/10.1109/RCAR.2017.8311867
17 D. Hongde, Z. Weiwei, Z. Baidong, D. Shaowu, and W. Rui: J. Beijing University of Aeronautics and Astronautics **47** (2021) 1959. https://doi.org/10.13700/j.bh.1001-5965.2020.0349

About the Authors

Xiaowen Cai received her Ph.D. degree in optical engineering with Beihang University, Beijing, China, in 2020. Since 2020, she has been working at Xiangtan University. Her research interests are related to inertial navigation and integrated navigation.

Fengjiao Guo received her B.S. degree from Hunan Institute of Engineering, China, in 2023 and has been studying at Xiangtan University, School of Automation and Electronic Information, majoring in the Electronic Information Program. Her research interests are in MEMS, indoor positioning systems, sensors,and their applications in Internet of Things (IoT) and wearable technology.

Qiaoting Gong received her B.S. degree from Hunan City University, China, in 2021 and has been studying at Xiangtan University, School of Automation and Electronic Information, majoring in the Electronic Information Program. Her research interests are in MEMS, indoor positioning systems, and sensors.

Daifeng Zhang received her B.S. degree from Xiangtan University, China, in 2020 and her M.S. degrees from Xiangtan University, China, in 2023. From 2019 to 2023, she participated in several national scientific research projects. Her research interests are in MEMS, indoor positioning systems, and sensors.

Yangzhuo Chen received his master's degree from Xiangtan University. He is an experimentalist and works as a lecturer in Xiangtan University, and is mainly engaged in embedded development, UAVs, and control systems. (mufgqting@foxmail.com)

Pinchun Li received her B.S. degree from Xiangtan University, China, in 2022 and has been studying at Xiangtan University, School of Automation and Electronic Information, majoring in the Information and Communication Engineering Program. Her research interests are in MEMS, indoor positioning systems, and sensors.